Research Article | Vol. 31, No. 16 / 31 Jul 2023 / Optics Express 25398
Optics EXPRESS

Sensing the profile of particulate beam attenuation coefficient through a single-photon oceanic Raman lidar

MINGJIA SHANGGUAN,* ZHUOYANG LIAO, YIRUI GUO, AND ZHONGPING LEE

State Key Laboratory of Marine Environmental Science, College of Ocean and Earth Sciences, Xiamen University, Xiamen 361102, China
*mingjia@xmu.edu.cn

Abstract: A lidar technique has been proposed and demonstrated for remotely sensing particulate beam attenuation coefficient (c_p) profiles using the Raman backscattered signal from water. In Raman lidar, the backscatter coefficient at 180° can be considered constant, allowing for the determination of the lidar attenuation coefficient (K_{lidar}) from the Raman backscattered signal. This scheme has these features. 1) The bandwidth of the filter that used to extract the Raman component from the backscattered signal of the lidar was optimized to ensure sufficient lidar signal strength while minimizing the influence of chlorophyll fluorescence on inversion. 2) A receiving telescope with narrow field of view (FOV) and small aperture was utilized to suppress multi-scattering components in the backscattered signal. 3) A relationship between the beam attenuation coefficient (c) and K_{lidar} was established after simulations via a semi-analytic Monto Carlo. 4) The value of c_p was obtained by subtracting the attenuation coefficient of pure seawater (c_w) from c. According to the theoretical analysis, the maximum relative error of c_p is less than 15% for chlorophyll concentrations up to 10 mg/m^3. Due to the water Raman backscattered signal being several orders of magnitude lower than the elastic backscattered signal, a single-photon detector is required to significantly improve the detection sensitivity to the single-photon level. To validate this approach, a field experiment was conducted aboard the R/V Tan Kah Kee in the South China Sea from September 4th to September 5th, 2022, and continuous subsurface profiles of c_p were obtained. These measurements confirm the robustness and reliability of the oceanic single-photon Raman lidar system and the inversion method.

1. Introduction

The particulate beam attenuation coefficient (c_p) is a crucial parameter in oceanography. It quantifies the rate at which light beam is absorbed and scattered by particles suspended in seawater, which affects the propagation of light and the amount of energy available for photosynthesis and other biological processes. Since c_p is closely related to the concentration, size, shape, and composition of particles in the water column, it provides valuable information on the physical and biogeochemical properties of marine ecosystems.

One of the key applications of c_p in ocean science is its use in estimating the amount of particulate organic carbon (POC) in the water column, which is a major component of the oceanic carbon cycle [1]. POC is an important constituent of carbon budgets in the ocean, being produced by primary producers such as phytoplankton and exported to the deep ocean through sinking and vertical mixing processes. The concentration of POC in seawater can be challenging to measure directly, but several indirect methods have been developed based on the relationship between c_p and POC. Numerous studies have demonstrated a strong relationship between c_p and POC in certain regions of the ocean [2–4]. It is now well established that c_p is a useful proxy for estimating POC concentrations from remote sensing and in situ measurements.

#493660 https://doi.org/10.1364/OE.493660
Journal © 2023 Received 19 Apr 2023; revised 14 Jun 2023; accepted 22 Jun 2023; published 17 Jul 2023

Optics EXPRESS

Over the years, various technologies have been developed to measure c of water, from which c_p can be obtained by subtracting the contribution of pure seawater (c_w). These technologies include the Beer-Lambert law, the stimulated Brillouin scattering, transmissometer method, and spectrophotometric method, among others [5–7]. While in situ measurements offer high accuracy, they are constrained by their limited spatial coverage and shallow depth range, which can hinder their ability to capture the large-scale variability and dynamics of marine systems. On the other hand, remote sensing provides an efficient way to monitor changes in c of water over time and space, making it a valuable tool for environmental management and research.

However, accurately retrieving c through remote sensing techniques, both passive and active, is still a challenging task [8–10]. One approach is to use the chlorophyll concentration (Chl) that derived from passive ocean color remote sensing [11]. However, this approach can be limited by the influence of physiological processes, such as changes in intracellular pigmentation, as well as the absence of an accurate indicator of non-phytoplankton particle populations. Another approach for estimating c involves using lidar depolarization measurements and diffuse attenuation coefficients (K_d), which can be obtained from ocean color products or Brillouin lidar measurements [9]. However, simultaneous acquisitions of high-precision lidar depolarization and K_d using satellite sensors remain a challenge.

Fortunately, as an active technique, lidar has the capability to measure time-resolved backscattered and forward-scatter photon contributions arriving at the detector, making it an important technique for remote sensing of oceanic parameters such as particulate backscattering, size spectrum, and vertical distribution of ocean particles [12]. Despite its potential benefits, it remains a challenge using oceanic lidars in accurately retrieving c. The primary challenge lies in accurately inverting the lidar attenuation coefficient (K_{lidar}), with the second challenge being the calculation of c or K_d from K_{lidar}. Tremendous efforts have been devoted to developing advanced algorithms [13] and updating the hardware of lidar [14,15].

One major limitation of an elastic backscatter lidar is that it faces an ill-posed mathematic problem, as it needs to infer two unknowns, namely, attenuation coefficient (K_{lidar}) and backscatter coefficient at 180° (β), from a single measurement. Numerous attempts have been made to resolve this inherent ill-posed problem in the lidar equation. Initially, various algorithms have been proposed without changing the mechanism of elastic backscatter lidar, including the slope method [16], Klett method [17], Fernald method [18] and perturbation method [19], among others. Nevertheless, each method is based on a set of assumptions that may not be perfect, leading to certain levels of inverse error. An important leap in retrieval accuracy has been achieved with the high spectral-resolution lidar (HSRL) technique, which can independently measure backscattering and attenuation by separating the particulate and molecular backscatters in wavelength distribution [20,21]. Recently, by combination the HSRL technique and a developed multiple scattering correction algorithm, K_d can be estimated accurately [15]. However, the complexity of the HSRL system and its high requirements for frequency stability limit its implementation and operation to some extent.

Compared to HSRL, Raman lidar systems are easier to implement and maintain. While a Raman lidar has been proposed and utilized to profile atmospheric attenuation coefficient [22], its application in remote sensing of oceanic optical parameters is still limited [23,24]. In this work, an oceanic Raman lidar is proposed and demonstrated for remotely sensing the c_p profiles. In Raman lidar, β can be treated as a constant value [22]. Therefore, analyzing of the Raman lidar signal alone permits the determination of K_{lidar}. On the other hand, to overcome the disadvantage that the intensity of Raman backscattered signals is 2-3 orders of magnitude lower than the elastic backscattered signals, a single-photon detector is required to enhance the detection sensitivity to a single-photon level. The single-photon detector technique has been widely applied in atmospheric and target imaging [25–27], but its application in oceanic lidar is limited [28–30], particularly in oceanic Raman lidar.

Optics EXPRESS

After acquiring K_{lidar}, the next challenge is to invert the values of c from the K_{lidar} data. Based on Monte Carlo (MC) simulation, researches have concluded that K_{lidar} is determined by c when lidar backscattered signal is dominated by quasi-single scattering, while K_{lidar} is given by K_d when backscattered signal is dominated by multi-scattering [31]. Based on these findings, in this work, an all-fiber connected Raman lidar with a receiver telescope with narrow FOV (2.1 mrad) and small aperture (22 mm) was developed to suppress the multi-scatter components in backscattered lidar signal. Finally, with a relationship between c and K_{lidar} establish by MC simulations, c can be estimated from K_{lidar}. The organization of this article is as follows: Firstly, an introduction to methodology is presented, including principles and an analysis of potential influencing factors. Next, the MC method is introduced to establish the relationship between c and K_{lidar}. Finally, a field experiment is introduced, which validate the robustness and feasibility of this approach and the lidar system.

2. Methodology

Let the Raman lidar equation be written as follows:

$$P_w(\lambda, z) = K \cdot O(z + n \cdot h)\beta_t \exp\left\{-\int_0^z K^t_{lidar}(\lambda_L, \lambda,\ \xi)\, d\xi\right\} \Big/ (z + n \cdot h)^2 \tag{1}$$

where P_w represents the water Raman backscattered signal at a depth of z; h represents the height at which the lidar is located above the water surface, which in this case is 15 m; λ_L denotes the wavelength of the transmitting laser, which is 532 nm; λ represents wavelength of Raman signal emitted by water; K is a constant that includes parameters that are independent of depth such as the output laser power, quantum efficiency of the detector, and transmittance of the optical system for both the transmitted and received signals; $O(z+n \cdot h)$ is the overlap function [32]; n is the index of refraction of water; β_t represents the total backscatter coefficient at 180° at 650 nm, which includes both the Raman backscatter coefficient at 180° of water (defined as β_R) and the backscatter coefficient at 180° of chlorophyll fluorescence (defined as β_F) at this wavelength; $K^t{}_{lidar}$ is the round-trip attenuation coefficient of lidar, including the attenuation coefficients of downwelling $K_{lidar}(532, z)$ and upwelling $K_{lidar}(650, z)$.

β_t can be represented by the following equation:

$$\beta_t = \beta_R + \beta_F \tag{2}$$

Assuming that β_t is dominated by β_R, while the influence of β_F can be neglected (the error caused by this assumption will be analyzed in detail in section 4.1). Since the density of seawater varies slightly with depth within the subsurface water (≤15 m) [33], the influence of density on β_R can be considered negligible in this work. Then, β_R can be expressed as follows [34]:

$$\beta_R(\lambda) = b_R(\lambda_L, \lambda) \cdot f_R(\lambda_L, \lambda) \cdot \tilde{\beta}_R(\pi) \tag{3}$$

where b_R is the Raman scattering coefficient of the water molecules, which tells how much of the irradiance at the excitation wavelength λ_L scatters into all emission wavelengths λ; f_R is the Raman wavelength redistribution function; $\tilde{\beta}_R(\pi)$ is the Raman scattering phase function. It should be noted that since β_R is only related to water molecules and can be considered constant [34], the two unknowns in the lidar equation, β_R and K_{lidar}, can be reduced to only one unknown, K_{lidar}. This is the reason why a Raman lidar can accurately invert K_{lidar}.

When the Raman backscattered signal passes through a Raman filter, it can be expressed as the convolution of the Raman backscattered signal P_w and the transmission function of the filter,

Optics EXPRESS

as shown in the following equation:

$$P_m(z) = P_w(z) \otimes g(\lambda, \sigma) \tag{4}$$

where $g(\lambda, \sigma)$ is the transmittance function of the filter, which can be represented by a Gaussian function in this work, namely,

$$g(\lambda, \sigma) = 1/(\sigma\sqrt{2\pi}) \exp[-\lambda^2/(2\sigma^2)] \tag{5}$$

where σ is its standard deviation, which can be expressed as $FWHM/2\sqrt{\ln 4}$, and $FWHM$ is the full width at half maximum of the Raman filter.

When the geometric overlap factor $O(z)$ beneath the water surface is equal to 1, $K^t{}_{lidar}$ can be calculated using a simple slope method, as follows:

$$K^t_{lidar}(\ z) = \frac{d}{dz}\left\{\ln\left[\frac{1}{P_m(z)\cdot(z + n\cdot h)^2}\right]\right\} \tag{6}$$

Then, through a semi-analytic MC simulation, which will be described in section 5, the relationship between $K^t{}_{lidar}$ and the total beam attenuation coefficient can be established as follows:

$$c^t(z) = \exp\{m\cdot[K^t_{lidar}(z)]^2 + n\cdot K^t_{lidar}(z) + t\} \tag{7}$$

where m, n and t are fitted parameters. It should be noted that c^t(z) is the sum of the beam attenuation coefficients c at the transmitted wavelength of 532 nm and the received wavelength of 650 nm, namely,

$$c^t(z) = c(532, z) + c(650, z) \tag{8}$$

where c can be expressed as the sum of the absorption coefficient (a) and scattering coefficient (b). By separating the particle contribution and the pure water contribution in c, c^t can also be expressed as:

$$c^t(z) = c^t_p(z) + c^t_w \tag{9}$$

c^t_w is the sum of the beam attenuation coefficients of pure water at 532 nm and 650 nm, which can be regarded as a constant. Similarly, c^t_p represents the sum of the particulate beam attenuation coefficients at 532 nm and 650 nm. By substituting Eq. (9) into Eq. (7), c^t_p can be obtained as follows:

$$c^t_p(z) = \exp[m\cdot K^t_{lidar}(z)^2 + n\cdot K^t_{lidar}(z) + t] - c^t_w \tag{10}$$

Subsequently, the particulate beam attenuation coefficient at 532 nm, namely c_p (532, z), is obtained through the ratio of particulate beam attenuation coefficients ($r_{650/532}$), which can be expressed as:

$$r_{650/532} = c_p(650, z)/c_p(532, z) \tag{11}$$

Several models for the inherent optical properties (IOPs) of water bodies [35–41] have revealed that, for both Case 1 and Case 2 waters, the ratio $r_{650/532}$ only exhibits a small range for chlorophyll concentration (Chl) varying between 0.01 mg/m^3 and 10 mg/m^3 (further details regarding this will be provided in section 4.1). Thus, the profile c_p (532, z) can be expressed as:

$$c_p(532,\ z) = \{\exp[m\cdot K^t_{lidar}(z)^2 + n\cdot K^t_{lidar}(z) + t] - c^t_w\}/(1 + r_{650/532}) \tag{12}$$

To provide a clear overview of the inversion process, Fig. 1 provides a complete flowchart of the inversion process.

Optics EXPRESS

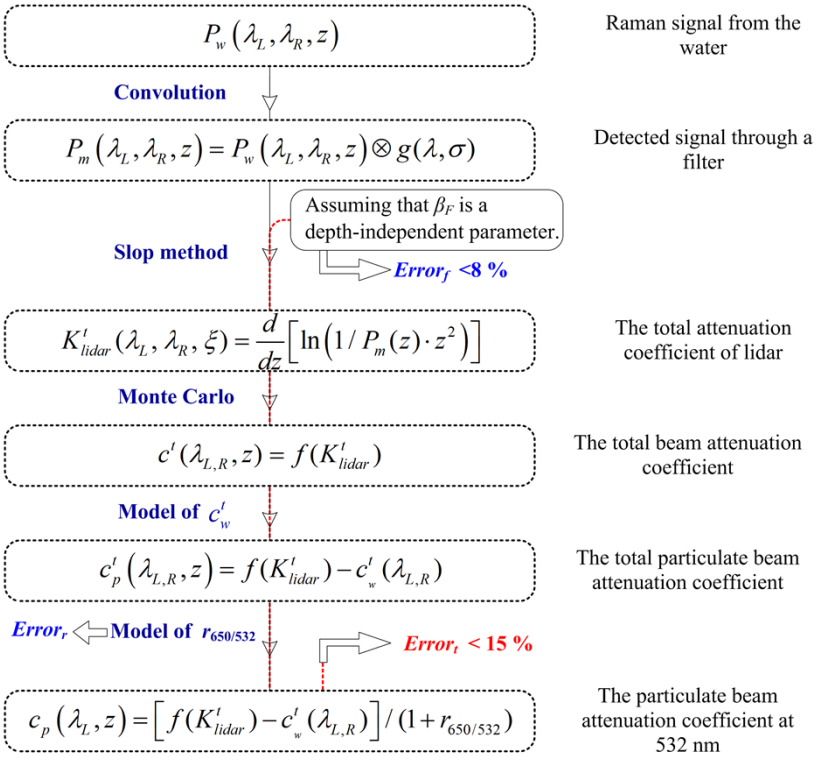

Fig. 1. Flowchart of the inversion process.

3. Optimization of the bandwidth of the Raman filter

Based on Eq. (4), it is evident that the intensity of the backscattered signal is influenced by the shape and bandwidth of the filter after it passes through the filter. The primary impact of the filter on the backscattered signal is reflected in its effect on β_t [25]. This effect can be analyzed using β'_t, which is mathematically expressed as follows:

$$\beta'_t = \beta_t \otimes g(\lambda, \sigma) = \beta_R \otimes g(\lambda, \sigma) + \beta_F \otimes g(\lambda, \sigma) \tag{13}$$

To simplify the analysis of the impact of the filter transmission function on β_R and β_F, we define $\beta'_R = \beta_R \otimes g(\lambda, \sigma)$ and $\beta'_F = \beta_F \otimes g(\lambda, \sigma)$, where β_R is obtained from Eq. (3). It should be noted that the center wavelengths of Raman scattering and fluorescence scattering are different, with respective values of 650 nm and 685 nm. Additionally, in order to simplify the analysis, a model for chlorophyll fluorescence is applied to calculate β_F when only considering chlorophyll fluorescence and ignoring fluorescence from other substances in the water. This model is applicable in Case 1 water, where the inherent optical properties can be adequately described by phytoplankton (represented by chlorophyll concentration, or Chl). The effect of fluorescence from other substances on the inversion will be studied in our future work. Then, β_F can be expressed as [42]:

$$\beta_F(\lambda, \mathrm{Chl}) = a_{ph}(532, \mathrm{Chl}) \cdot \Phi_C \frac{532}{\lambda} h_C(\lambda) \cdot \frac{1}{4\pi} \tag{14}$$

where $a_{ph}(532, \mathrm{Chl})$ is the chlorophyll absorption coefficient at the excitation wavelength of 532 nm, which can be obtained from Bricaud's model for a given Chl [43]; Φ_C is the quantum efficiency for chlorophyll fluorescence, with a value between 0.005 and 0.07 [44], and 0.06 being

Optics EXPRESS

used in this study; h_C denotes the chlorophyll fluorescence wavelength emission function from the model [45]. Further, a_{ph} (532, Chl) and $h_C(\lambda)$ can be mathematically expressed as:

$$a_{ph}(532, \mathrm{Chl}) = 0.0113 \cdot \mathrm{Chl}^{0.871} \tag{15}$$

$$h_C(\lambda) = W\sqrt{\frac{4\ln 2}{\pi}}\frac{1}{25}\exp[-4\ln 2(\frac{\lambda-685}{25})^2] + (1-W)\sqrt{\frac{4\ln 2}{\pi}}\frac{1}{50}\exp[-4\ln 2(\frac{\lambda-730}{50})^2] \tag{16}$$

where W represents the weight of the Gaussians, which is set as 0.75 in this study.

The effect of filter bandwidth on β'_R is first analyzed, as shown in Fig. 2(a). it can be seen that the larger the bandwidth, the stronger the Raman backscattered signal, as indicated by the increasing value of β'_R. Therefore, on one hand, using a larger filter bandwidth is advantageous for improving the signal-to-noise ratio (SNR) of the detection. On the other hand, a larger bandwidth also results in more chlorophyll fluorescence being detected in the lidar backscattered signal, as shown in Eq. (13). This increase in fluorescence causes the assumption of a constant β_t to no longer hold, introducing errors in the inversion of c_p.

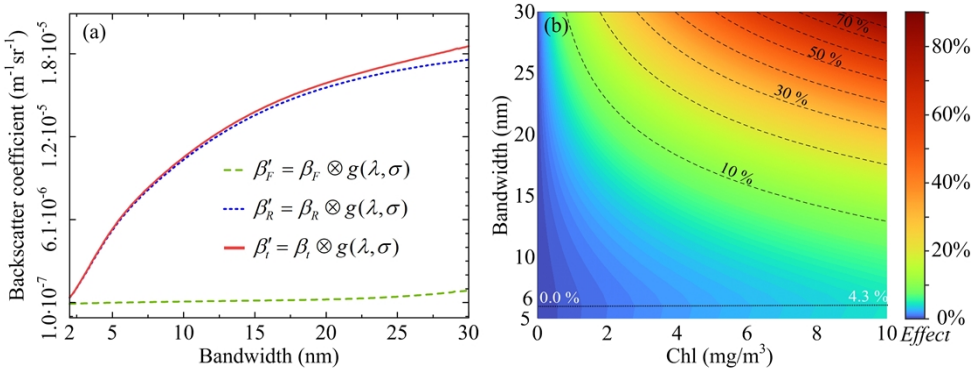

Fig. 2. (a) Effect of the bandwidth of Raman filter on backscatter coefficient at 180°, (b) effect of filter bandwidth on β'_t for the Chl ranging from 0.01 to 10 mg/m^3.

Then, the effect of filter bandwidth on β'_t is analyzed as follows:

$$Effect = [\beta'_t(650, \sigma, Chl) - \beta'_t(650, \sigma, 0.01)]/\beta'_t(650, \sigma, 0.01) \times 100\% \tag{17}$$

where β'_t (650, σ, 0.01) is a reference value when Chl is set to 0.01 mg/m^3. As shown in Fig. 2(b), an increase in the filter bandwidth and an increase in Chl both lead to a larger relative error in β'_t.

To minimize the influence of chlorophyll fluorescence while maintaining the strength of the Raman backscattered signal, the bandwidth of the Raman filter was optimized. Finally, a bandwidth of 6 nm was selected to guarantee that the effect of chlorophyll fluorescence on β'_t remained below 5% for Chl ranging from 0.01 to 10 mg/m^3.

4. Analysis of the effects of $r_{650/532}$ and chlorophyll fluorescence on c_p(532) inversion

4.1. $r_{650/532}$ effect

As described in the methodology section, determining the $r_{650/532}$ ratio is crucial for calculating c_p(532) from c^t data. In this study, we utilized the IOPs model for Case 1 waters and measured data from Case 2 waters to investigate the variation of $r_{650/532}$ in different water bodies. Previous

Optics EXPRESS

researches have extensively investigated the IOPs of Case 1 waters, which are primarily influenced by phytoplankton, as initially proposed by Morel and Prieur in 1977 [46] and is still widely adopted today. In this study, we employed two empirical relationships to calculate the particulate absorption coefficient (a_p) [35,36,41], and four empirical relationships to calculate the particulate scattering coefficient (b_p) [37–40], as listed in Table 1. Figure 3(a) shows the spectrogram of c_p from 400 nm to 700 nm, with Chl ranging from 0.01 to nearly 60.0 mg/m^3. In most Case 1 waters, Chl ranges from 0.01 to 1.00 mg/m^3 [47–49]. However, to illustrate the distribution of $r_{650/532}$ in Case 2 waters with high Chl, we extended Chl up to nearly 30.0 mg/m^3.

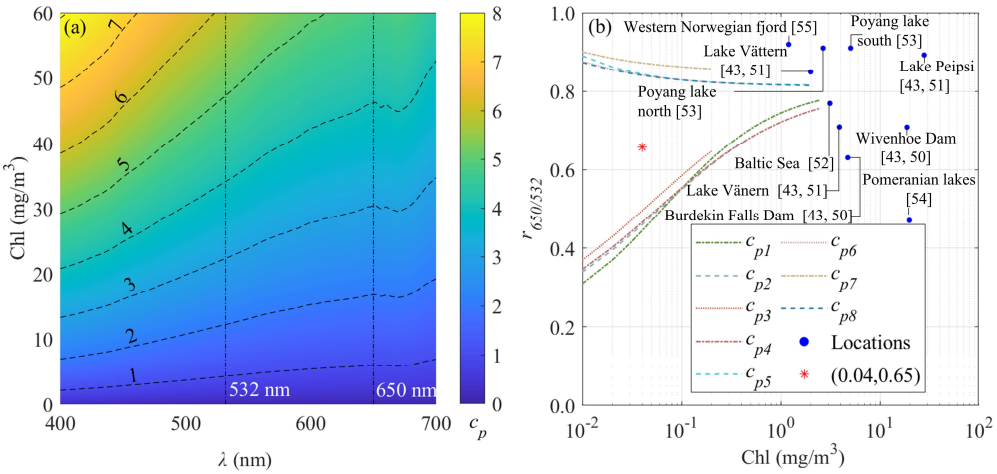

Fig. 3. (a) Spectrogram of the c_p under varying Chl, (b) distribution of $r_{650/532}$ in case 1 water (lines) and case 2 water (circles). c_{p1} is the sum of a_{p1} and b_{p1}; c_{p2} is the sum of a_{p1} and b_{p2}; c_{p3} is the sum of a_{p1} and b_{p3}; c_{p4} is the sum of a_{p1} and b_{p4}; c_{p5} is the sum of a_{p2} and b_{p1}; c_{p6} is the sum of a_{p2} and b_{p2}; c_{p7} is the sum of a_{p2} and b_{p3}; c_{p8} is the sum of a_{p2} and b_{p4} [Refs. 50–55].

Table 1. Absorption and scattering coefficients of particles in case 1 water.

Empirical relationships of a_p and b_p	Applicable range of Chl	References
$a_{p1}(\lambda) = A_p(\lambda) \cdot \mathrm{Chl}^{E_p(\lambda)}$	0.02 ~ 25 mg/m^3	[35,36]
$a_{p2}(\lambda) = 0.06A(\lambda) \cdot \mathrm{Chl}^{0.65}$	0.02 ~ 20 mg/m^3	[41]
$b_{p1}(\lambda) = 0.416 \cdot 550 \cdot \mathrm{Chl}^{0.766}/\lambda$	0.02 ~ > 30 mg/m^3	[37]
$b_{p2}(\lambda) = 0.252 \cdot 660 \cdot \mathrm{Chl}^{0.635}/\lambda$	~0.01 ~ 4.5 mg/m^3	[39]
$b_{p3}(\lambda) = [0.309 - 0.000384(\lambda - 550)] \cdot \mathrm{Chl}^{0.60}$	~0.02 ~ 2 mg/m^3	[38]
$b_{p4}(\lambda) = 0.3 \cdot 550 \cdot \mathrm{Chl}^{0.62}/\lambda$	0.01 ~ 30 mg/m^3	[40]

By combining two sets of empirical relationships for parameters a_p [35,36,41] and b_p [37–40], we generated eight different models for parameter c_p. These models were used to calculate the $r_{650/532}$ ratio at different Chl levels, as shown by the dashed lines in Fig. 3(b). As shown in Fig. 3(b), the $r_{650/532}$ ratio tends to stabilize as Chl increases, especially when Chl exceeds 3 mg/m^3. However, for oceanic waters with relatively low Chl concentrations, $r_{650/532}$ exhibits a significant relative variation with changes in Chl.

In contrast to Case 1 waters, c_p in Case 2 waters is not solely determined by Chl. We analyzed the variations in $r_{650/532}$ at ten different locations in Case 2 waters, and their corresponding values versus Chl are illustrated by circles in Fig. 3(b). Detailed information on the specific

Optics EXPRESS

locations and relevant references is also provided in Fig. 3(b). The minimum and maximum values of $r_{650/532}$ for Case 2 waters are 0.47 and 0.92, respectively, with corresponding Chl values of 19.8 mg/m^3 and 1.2 mg/m^3. The range of variation in $r_{650/532}$ determined through this analysis is employed to investigate the impact of changes in the $r_{650/532}$ value on the inversion of c_p.

Based on the previous analysis, it is evident that the value of $r_{650/532}$ actually varies with Chl. However, in the inversion process, we assume it to be a fixed value due to the lack of prior knowledge on Chl. Assuming that the ratio of particulate beam attenuation coefficients used in the inversion process is $r'_{650/532}$, and the corresponding particulate beam attenuation coefficient obtained from the inversion is $c_p(r'_{650/532})$, the relative deviation between $c_p(r'_{650/532})$ and the true ground of $c_p(r_{650/532})$ can be expressed as follows:

$$Error_r = [c_p(532,\ r'_{650/532}) - c_p(532, r_{650/532})]/c_p(532, r_{650/532}) \tag{18}$$

Combined with Eq. (12) in the methodology section, $Error_r$ can be simplified as:

$$Error_r = \{[1/(1 + r'_{650/532})] - [1/(1 + r_{650/532})]\}/[1/(1 + r_{650/532})] \times 100\ \% \tag{19}$$

The distribution of $Error_r$, when the value of $r'_{650/532}$ used in the inversion process, varies from 0.45 to 0.9, and the true ground value of $r_{650/532}$ also varies within this range, is shown in Fig. 4(a). The results indicate that the $Error_r$ is small when $r'_{650/532}$ is close to $r_{650/532}$, and the error increases as the deviation between $r'_{650/532}$ and $r_{650/532}$ becomes larger. However, the $Error_r$ remains within the range of -23.7% to 31.0%. in this work, $r'_{650/532}$ is set to 0.65, and $Error_r$ ranges from -12.1% to 15.2%, as shown in Fig. 4(b).

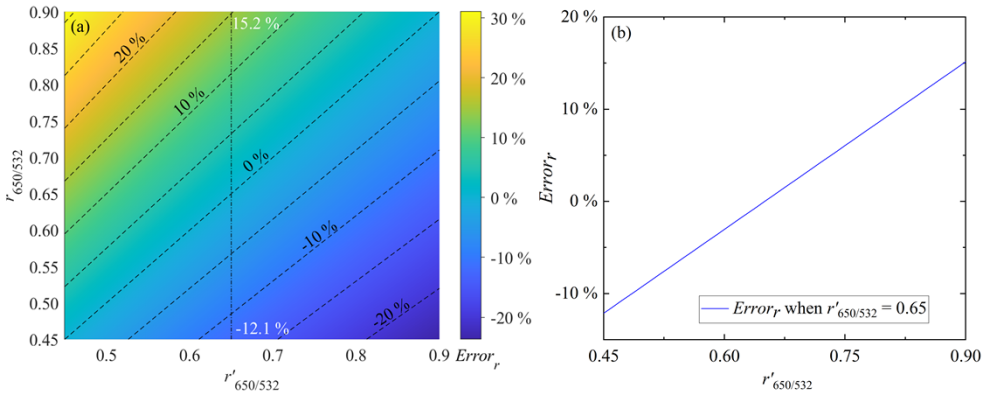

Fig. 4. The estimated error caused by the change of the ratio $r_{650/532}$ to the inversion of c_p.

4.2. β_F effect

In this section, we will analyze the error that arises from neglecting the vertical variation of the backscattered coefficient of chlorophyll fluorescence β_F during the inversion of c_p. Firstly, four typical Chl profiles were obtained, including open-ocean, mid-latitude case 1 water, lakes, and water surrounding Europe [56–59]. These water bodies were chosen to represent a diverse range of non-uniform aquatic environments and their associated chlorophyll distributions. Then, $c_p(532, \text{Chl})$ was calculated based on models using Chl profiles [35–41]. According to Eq. (9) and Eq. (11), c^t can be expressed as a function of c_p as follows:

$$c^t = (1 + r_{650/532})c_p(532, \text{Chl}) + c^t_w(\lambda_{L,R}) \tag{20}$$

Then, $K^t{}_{lidar}$ was obtained by using the relationship between c^t and $K^t{}_{lidar}$ established based on the inverse function of Eq. (10). β_t was obtained by using Chl profile based on Eq. (2). Finally,

Optics EXPRESS

the normalized signal of the Raman lidar was simulated based on Eq. (1). Then, using the approach provided in the methodology section, the particulate beam attenuation coefficient can be obtained, defines as $c'_p(532, \mathrm{Chl})$. The deviation between the inversion and true values of the

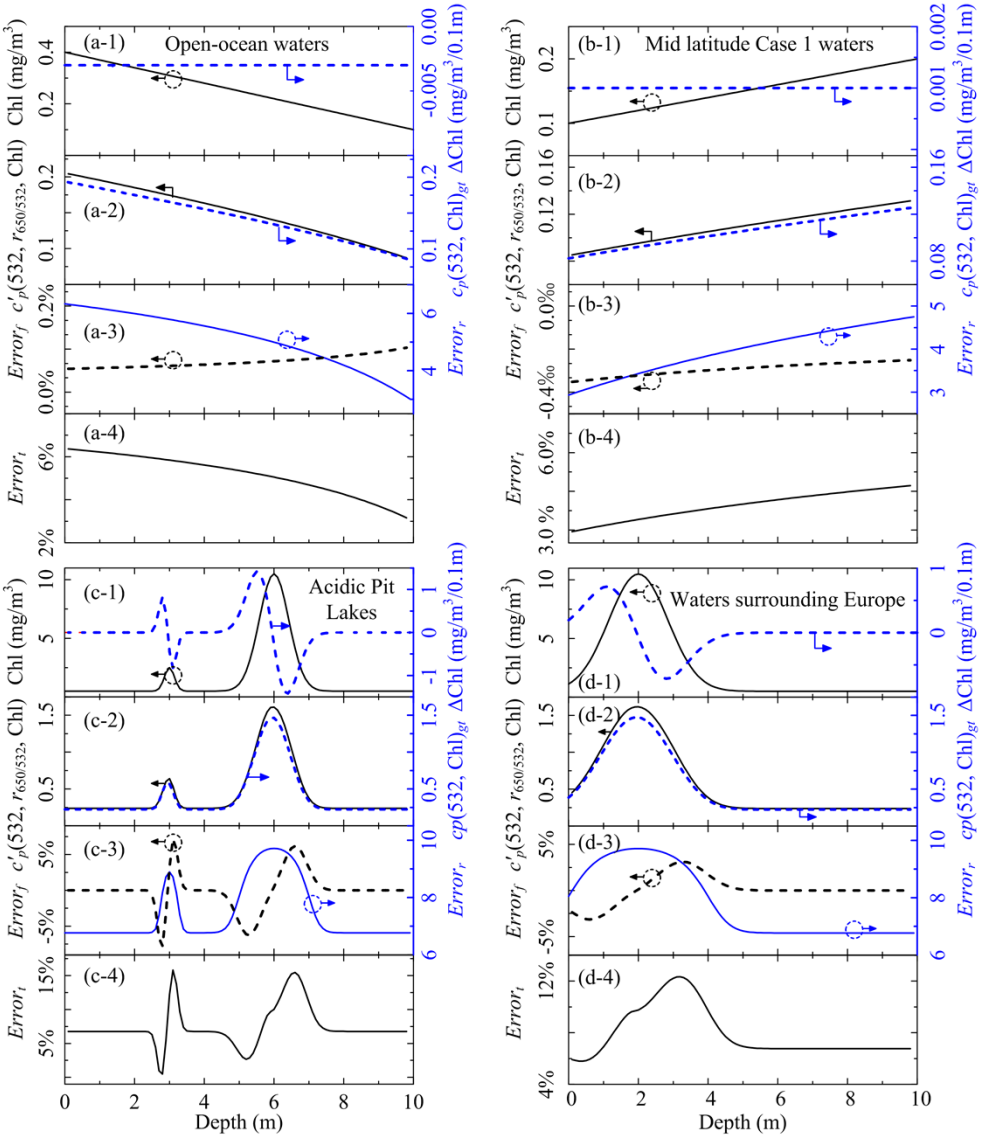

Fig. 5. Theoretical analysis of errors. The sub-figures (a)-(d) show different chlorophyll vertical distribution, including (a) linearly decreasing [56], (b) linearly increasing [59], (c) bimodal with two Gaussian distribution [58], and (d) unimodal with a single Gaussian distribution [57]. Each sub-figure comprises three panels, with the top showing the corresponding Chl vertical distribution and relative Chl difference between adjacent depth intervals (ΔChl). The second panel provides the inversed c'_p and its ground true c_p, while the third panel displays the $Error_f$ and $Error_r$ distribution. The bottom panel shows the $Error_t$ distribution.

Optics EXPRESS

particulate beam attenuation coefficient can be estimated as follows:

$$Error_f = [c'_p(532,\ \mathrm{Chl}) - c_p(532,\ \mathrm{Chl})_{gt}]/c_p(532,\ \mathrm{Chl})_{gt} \times 100\% \tag{21}$$

where $c_p(532, \mathrm{Chl})_{gt}$ is the true value calculated by the models provided in Table 1, with the provided Chl profiles.

In the above evaluation process, the same value of $r_{650/532}$ was used to generate the lidar backscattered signal from the known vertical distribution of Chl and to invert $c_p(532, \mathrm{Chl})$ from the lidar backscattered signal. Therefore, this relative deviation only considers the effect of Chl variation on β_t, but does not consider the effect of $r_{650/532}$ on the inversion.

To take the effect of $r_{650/532}$ into account, $r_{650/532}$ is no longer considered a constant but a variable related to the vertical profiles of Chl when using the vertical profile of Chl to generate the lidar backscattered signal. Based on this backscattered signal and using the same inversion method as described above, the particulate beam attenuation coefficient can be obtained, defined as $c'_p(532, r_{650/532}, \mathrm{Chl})$. In this case, the relative deviation between the inverted value $c'_p(532, r_{650/532}, \mathrm{Chl})$ and the true value $c_p(532, \mathrm{Chl})_{gt}$ can be considered as a total error, defined as $Error_t$, which takes into account both the influence of the vertical distribution of Chl on β_t and $r_{650/532}$. It can be expressed as follows:

$$Error_t = [c'_p(532,\ r_{650/532},\ Chl) - c_p(532,\ Chl)_{gt}]/c_p(532,\ Chl)_{gt} \times 100\% \tag{22}$$

Figure 5 presents the distribution of three types of errors, namely $Error_r$, $Error_f$, and $Error_t$ under various Chl vertical distributions. As shown in Fig. 5(a) and Fig. 5(b), when there is a monotonic change in Chl, whether increasing or decreasing, the errors increase with an increase in Chl. In such cases, $Error_t$ is primarily influenced by $Error_r$, and the total error $Error_t$ remains below 10%. On the other hand, when there is a layered distribution of Chl, $Error_t$ is primarily attributed to $Error_r$ when Chl is low or relatively stable. On the other hand, when there is a layered distribution of Chl, as shown in Fig. 5(c) and Fig. 5(d), $Error_t$ is primarily attributed to $Error_r$ when Chl is low or relatively stable. However, if Chl is high, both $Error_r$ and $Error_f$ contribute approximately equally to $Error_t$, and the magnitude of $Error_t$ increases with an increase in Chl variation rate, which is defined as ΔChl. Regarding $Error_f$, as shown in Fig. 5, especially in Fig. 5(c-3) and Fig. 5(d-3), even when the Chl varies significantly with depth, i.e., when β_F varies vertically, $Error_f$, as calculated using Eq. (21), can be controlled to be less than 8% due to the utilization of a narrow Raman filter with a bandwidth of 6 nm. Overall, in these four water types, the maximum value of $Error_t$ does not exceed 15%.

5. Monte Carlo simulation

MC simulation is a widely used tool in lidar simulation and has been extensively applied to simulate the backscattered signal of oceanic lidars [24]. In this study, a brief introduction is provided to the MC-based simulation of Raman lidar backscattered signals, without going into specific details. For more information on the simulation process, recent articles can be referred to [24,60].

The MC is used to simulate the random trajectories of photon propagation in a medium. The step and direction of photon trajectories depend on the scattering and absorption properties of the medium. Meanwhile, the MC method treats the photon as a typical particle and ignores its wave properties. The propagation of laser in water is treated as the combination of many photon trajectories. Laser energy attenuation is determined by three factors, namely the absorption of the medium, the scattering probability, and the probability distribution of the steps. To enhance the utilization efficiency of individual photons, a semi-analytic MC model is applied. This model enables every photon in the telescope FOV to return its expected value of energy and record its position [61,62]. Due to the weak intensity of Raman signals, only the first-order Raman signals

Optics EXPRESS

that arise from the initial laser wavelength are considered, while the second-order Raman that result from the first-order Raman signals are disregarded. The simulated lidar backscattered signal is dependent not only on the IOPs of the water, but also on the hardware and geometric parameters of the lidar. Table 2 presents the instrument parameters of the Raman lidar used as input in the MC simulation. It should be noted that the instrument parameters used in MC are the parameters of the actual shipborne Raman lidar.

Table 2. Input parameters of lidar system

	Parameter	Value
Pulsed laser	Radius of laser beam	2 mm
	Laser divergence angle	0.5 mrad
Coupler	Diameter of telescope	22 mm
	FOV of telescope	2.1 mrad
	Distance between emission axis and reception axis	15 mm
Scattering phase function	Petzold phase function [63]	
	Morel phase function [64]	
Other parameters	Height above the water surface	15 m
	Number of photons	10^8
	Sampling interval	100 mm

The absorption and scattering coefficients are modeled as follows:

$$a(\lambda) = a_w(\lambda) + 0.06A(\lambda) \cdot \mathrm{Chl}^{0.65} + a_y(\lambda) \tag{23}$$

$$b(\lambda) = b_w(\lambda) + b_p(\lambda) \tag{24}$$

where a_w is the absorption coefficient of pure seawater [65], A is the normalized spectral absorption values of phytoplankton pigments, a_y is the absorption coefficient of yellow substance, b_w is the scattering coefficient of pure water [66]. Table 3 provides the model used in MC simulation.

Table 3. The models used in MC simulation

Empirical relationships of coefficients	Applicable range of Chl	References
a_w and A is obtained through linear interpolation	0.2-18.4 mg/m^3	[65]
$\begin{cases} a_y(\lambda) = a_y(440)\exp[-0.014(\lambda - 440)] \\ a_y(440) = 0.2[a_w(440) + 0.06A(440) \cdot \mathrm{Chl}^{0.65}] \end{cases}$	0.02-20 mg/m^3	[67]
$b_w(\lambda) = 0.0046(450/\lambda)^{4.32}$	-	[66]
$b_R(\lambda) = 2.6 \times 10^{-4}(488/\lambda)^{5.5}$	-	[34]
$b_p(\lambda) = 0.3\mathrm{Chl}^{0.62}(550/\lambda)$	0.03-30 mg/m^3	[40]

In the simulation, two commonly used scattering phase functions were utilized, namely Petzold phase function and a phase function proposed by Morel et al. [63,64]. The sampling length is 20 m with a sampling interval is 0.1 m, resulting in a total of 200 sampling points for each simulation. To reduce the effects of multiple scattering in the lidar backscattered signal, a small aperture telescope with a limited FOV was employed. As illustrated in Fig. 6(a), the simulated signal exhibits an exponential decay. Based on statistical analysis of the lidar signal, the percentage of multiple scattering, represented by the second scattering and higher-order scattering, is low when Chl is low, and the lidar signal is dominated by single scattering. However, as Chl increases, the percentage of multiple scattering increases. By using the inversion method introduced by the

Optics EXPRESS

methodology section, K^t_{lidar} values for different Chls can be obtained. The relationship between c^t and K^t_{lidar} is shown in Fig. 6(b). After exponential fitting, the relationship between c_t and K^t_{lidar} is determined as:

$$c^t = \exp[-0.334 \cdot (K^t_{lidar})^2 + 1.916 \cdot K^t_{lidar} - 1.540] \tag{25}$$

From Fig. 6(b), it can be observed that when Chl is low (i.e., c^t is small and the lidar backscattered signal is dominated by single scattering), K^t_{lidar} is close to c^t. However, as Chl increases and the proportion of multiple scattering in the lidar backscattered signal increases, K^t_{lidar} becomes smaller than c^t and gradually deviates from the 1:1 line between K^t_{lidar} and c^t (as shown by the dashed line in Fig. 6(b)). However, there is still a strong correlation between K^t_{lidar} and c^t, as evidenced by a high coefficient of determination (R^2) of 0.99.

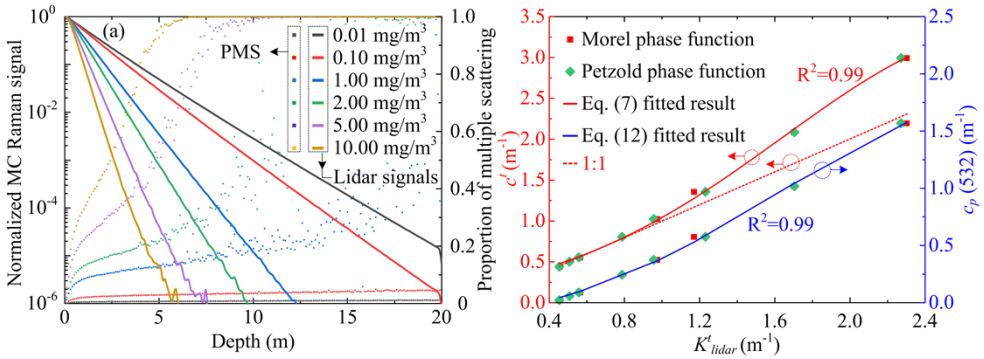

Fig. 6. (a) Simulation lidar backscattered signals (lines) and the corresponding proportion of multiple scattering (PMS) in the signals (scatters) for Chl ranging from 0.01 to 10 mg/m3, using the Morel phase function, (b) relationships between c^t and $c_p(532)$ with K^t_{lidar}, where scatter represents the results of MC simulations, and the solid line represents the results fitted by the formula.

6. Field experiment

6.1. Lidar system

Figure 7 illustrates a schematic diagram of the single-photon Raman lidar system setup, which consists four subsystems: a 532 nm pulsed laser, a transceiver, an optical receiver, and a data acquisition system. The system uses a compact fiber-based laser that follows a master oscillator power amplifier (MOPA) architecture, which utilizes a single-mode pulsed seed laser operating at 1064 nm. This seed laser is amplified through a single-mode ytterbium-doped fiber amplifier (SM-YDFA) and a high-power ytterbium-doped fiber amplifier (HP-YDFA) before passing through a lithium borate crystal (LBO) for second harmonic generation, resulting in up to an average power output of 1.0 W with a beam divergence of 0.5 mrad. The output pulse width is 3 ns, and the repetition frequency is 340 KHz.

To achieve a miniaturized and robust structure, a fiber-connected configuration is specifically designed for the Raman lidar system. In this configuration, the backscattered signal from water is coupled into a 105-μm multimode fiber (MMF) through a collimator with a 50.8 mm focal length, resulting in a narrow FOV of approximately 2.1 mrad. This narrow FOV not only provides significant suppression of backscattered noise but also suppresses multi-scattering components in the backscattered signal. The distance between the transmitted laser and the received collimator is approximately 15 mm. The backscattered Raman photons are extracted using a 45° dichroic mirror (DM) that reflects the elastic signal at 532 nm and transmits the signal from 550-670 nm,

Optics EXPRESS

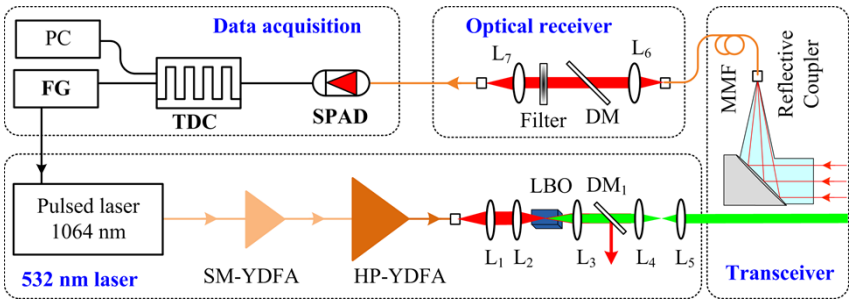

Fig. 7. Optical layout of the single-photon Raman lidar. SM-YDFA: Single-Mode Ytterbium-Doped Fiber Amplifier; HP-YDFA: High-Power Ytterbium-Doped Fiber Amplifier; L: lens; LBO: lithium borate; DM: dichroic mirror; MMF: Multimode fiber; SPAD: single-photon avalanche diode; TDC: time-to-digital converter; FG: function generator; PC: personal computer.

along with a bandpass Raman filter centered at 650 nm with a bandwidth (full width of half maximum) of 6 nm. By combining the DM with the Raman filter, the isolation degree of the 532 nm elastic backscattered signal can be achieved up to 55 dB, while the transmittance of the 650 nm Raman signal is > 80%. For photon detection, a compact silicon single-photon avalanche diode (SPAD) with an efficiency of approximately 52% and 100 dark counts per second (cps) at 650 nm is employed. The electronic module utilizes a self-built function generator (FG) using a Field Programmable Gate Array (FPGA) to generate precise control signals for the laser, the SPAD, and a self-designed time-to-digital converter (TDC). The TDC, with a resolution of 500 ps, is utilized for recording the timing information of pulse emission and photon detection. A summary of the system parameters is presented in Table 4.

Table 4. Key parameters of the Raman lidar system

	Parameter	Value
Pulsed laser	Wavelength	532 nm
	Pulse duration	3 ns
	Pulse energy	1 μJ
	Pulse repetition rate	340 KHz
Telescope	Focal length	50.8 mm
	Mode-field diameter of the MMF	105 μm
SAPD	Detection efficiency at 650 nm	52%
	Dark count	100 cps

6.2. *Field experiment*

To validate the effectiveness of the single-photon Raman lidar for retrieving c_p, a field experiment was conducted aboard the R/V Tan Kah Kee in the South China Sea from 8:38:04 PM on September 4th to 1:10:54 AM on September 5th, 2022. The lidar was installed on the deck of the research vessel, positioned approximately 15 m above the water surface, and the laser beam penetrated the water at a near-zenith angle of 0° after being reflected by a mirror located in front of the lidar. In this setup, the overlap function beneath the surface can be assumed to be 1.

Initially, the Raman lidar collected data with a time resolution of 1 second and a depth resolution of 0.5 ns, as shown in Fig. 8(a). To reduce inversion errors, the time resolution was adjusted to 15 seconds and the depth resolution was set to 1 m. The lidar signals was then multiplied by the

Optics EXPRESS

square of the corresponding sampling depth, followed by a logarithmic operation. $K^t{}_{lidar}$ profiles were calculated using the slope method, as provided in section 2. Subsequently, c^t profiles were derived based on the established relationship between c^t and $K^t{}_{lidar}$, as shown in Fig. 8(b). Finally, $c_p(532)$ profiles were obtained using the ratio $r_{650/532}$ (which was selected as 0.65), as illustrated in Fig. 8(c). While the filter combination can isolate elastic scattering by around 55 dB, it should be noted that the specular reflection on the water surface can still interfere with the Raman signal in the first 3 m. Therefore, the inversion results in Fig. 8(b) and 8(c) start from 3 m. In our future work, we will further improve the isolation of elastic scattering. The raw signal presented in Fig. 8(a) indicates the presence of a scattering layer beneath the sea surface, whose characteristics changed slowly during the R/V Tan Kah Kee cruise. By inverting $c_p(532)$, as shown in Fig. 8(c), variations can be clearly observed.

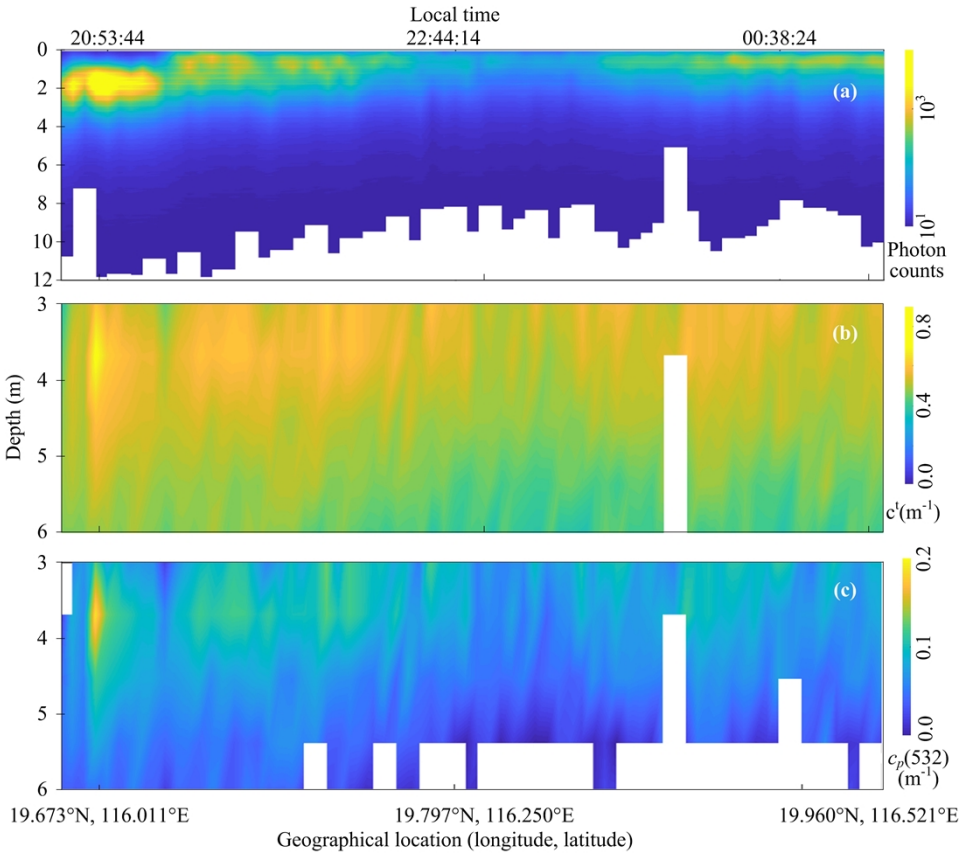

Fig. 8. Inversion results of the field experiment: (a) original $P_m(z)$; (b) profiles of c^t; (c) profiles of c_p (532).

7. Conclusion

In this work, we proposed a Raman lidar inversion method for measuring the profile of particulate beam attenuation coefficient, which remains a challenge for current remote sensing technologies. In Raman lidar, β can be treated as a constant value. Therefore, analysis of the Raman lidar signal alone permits the determination of $K^t{}_{lidar}$ by using a simple slope method. Furthermore, using the relationship between c^t and $K^t{}_{lidar}$, which was established by a semi-analytic MC mode,

Optics EXPRESS

c^t can be obtained. Finally, $c_p(532)$ can be obtained from c^t after assuming a ratio ($r_{650/532}$) of the particulate beam attenuation coefficient at two wavelengths.

In this work, systematic theoretical calculations were conducted, focusing on two main aspects. Firstly, the bandwidth of the Raman filter used to extract the Raman backscattered signal from water was optimized to 6 nm, which reduced the impact of chlorophyll fluorescence on $c_p(532)$ inversion while maintaining the intensity of the Raman backscattered signal. Secondly, an analysis was conducted to investigate the effects of $r_{650/532}$ and chlorophyll fluorescence on $c_p(532)$ inversion. The calculations showed that $Error_t$ is less than 15% when Chl falls within the range of 0.01-10 mg/m^3.

In terms of hardware design, a low-noise and high-efficiency single photon detector was adopted to enhance the performance of Raman lidar, enabling the detection of Raman backscattered profiles from water using a low-power laser. Additionally, a telescope with a small diameter and narrow FOV was designed to reduce the multiple scattering component in the lidar backscattered signal, resulting in K_{lidar} being closer to c. Ultimately, conducting field experiments served to validate the proposed method and demonstrate the feasibility and effectiveness of the Raman lidar in practical applications.

In future work, we plan to conduct a large number of comparative experiments to further validate our proposed method, comparing Raman lidar measurements with measurements obtained using in-situ methods. Additionally, more scattering phase functions will be used in the MC simulations to validate the established relationship between c^t and $K^t{}_{lidar}$. Moreover, to reduce the influence of chlorophyll fluorescence on the Raman backscattered signal, a laser with shorter wavelength, such as blue laser, will be considered as a transmitter. Once the effect of chlorophyll fluorescence on the Raman backscattered signal is reduced, the bandwidth of the Raman filter can be further increased, thus improving the SNR of the Raman backscattered signal. Furthermore, to enable the single-photon oceanic lidar to operate during daylight, this lidar will be integrated into an AUV platform in our future work. In summary, we believe that this work has significant potential, and the development of this technology will enable scientists to better study ocean carbon stocks and cycles, promoting a greater understanding of the role of the ocean in the global carbon cycle and the marine ecosystem as a whole.

Funding. National Key Research and Development Program of China (2022YFB3901704); Joint Funds of the National Natural Science Foundation of China (U2106210); Natural Science Foundation of Fujian Province (No. 2020J01026); MEL-RLAB Joint Fund for Marine Science & Technology Innovation.

Acknowledgment. We acknowledge the captain and crew of the R/V Tan Kah Kee for the help during the cruises.

Disclosures. The authors declare no conflicts of interest.

Data availability. The data that support the findings of this study are available from the corresponding author upon reasonable request.

References

1. M. J. Behrenfeld and E. Boss, "Beam attenuation and chlorophyll concentration as alternative optical indices of phytoplankton biomass," J. Mar. Res. **64**(3), 431–451 (2006).
2. W. Gardner, A. Mishonov, and M. Richardson, "Global POC concentrations from in-situ and satellite data," Deep Sea Res., Part II **53**(5-7), 718–740 (2006).
3. D. Stramski, R. A. Reynolds, M. Babin, S. Kaczmarek, M. R. Lewis, R. Röttgers, A. Sciandra, M. Stramska, M. Twardowski, and B. Franz, "Relationships between the surface concentration of particulate organic carbon and optical properties in the eastern South Pacific and eastern Atlantic Oceans," Biogeosciences **5**(1), 171–201 (2008).
4. M. Galí, M. Falls, H. Claustre, O. Aumont, and R. Bernardello, "Bridging the gaps between particulate backscattering measurements and modeled particulate organic carbon in the ocean," Biogeosciences **19**(4), 1245–1275 (2022).
5. M. Ouyang, J. Shi, L. Zhao, X. Chen, H. Jing, and D. Liu, "Real time measurement of the attenuation coefficient of water in open ocean based on stimulated Brillouin scattering," Appl. Phys. B **91**(2), 381–385 (2008).
6. M. S. Twardowski, J. M. Sullivan, P. L. Donaghay, and J. R. V. Zaneveld, "Microscale quantification of the absorption by dissolved and particulate material in coastal waters with an ac-9," J. Atmos. Oceanic Technol. **16**(6), 691–707 (1999).
7. N. Kozlova, A. Kozlova, and Z. A. Goreeva, "Spectrophotometric methods and their capabilities to study material optical parameters," in *2017 2nd International Ural Conference on Measurements (UralCon)*, (IEEE, 2017), 281–288.

Optics EXPRESS

8. E. Boss, W. H. Slade, M. Behrenfeld, and G. Dall'Olmo, "Acceptance angle effects on the beam attenuation in the ocean," Opt. Express **17**(3), 1535–1550 (2009).
9. Y. Hu, M. Behrenfeld, C. Hostetler, J. Pelon, C. Trepte, J. Hair, W. Slade, I. Cetinic, M. Vaughan, and X. Lu, "Ocean lidar measurements of beam attenuation and a roadmap to accurate phytoplankton biomass estimates," in *EPJ Web of Conferences*, (EDP Sciences, 2016), 22003.
10. G. Yang, Z. Tian, Z. Bi, Z. Cui, F. Sun, and Q. Liu, "Measurement of the Attenuation Coefficient in Fresh Water Using the Adjacent Frame Difference Method," in *Photonics*, (MDPI, 2022), 713.
11. K. J. Voss, "A spectral model of the beam attenuation coefficient in the ocean and coastal areas," Limnol. Oceanogr. **37**(3), 501–509 (1992).
12. J. H. Churnside and J. A. Shaw, "Lidar remote sensing of the aquatic environment," Appl. Opt. **59**(10), C92–C99 (2020).
13. Z. Zhang, P. Chen, C. Jamet, D. Dionisi, Y. Hu, X. Lu, and D. Pan, "Retrieving bbp and POC from CALIOP: A deep neural network approach," Remote Sens. Environ. **287**, 113482 (2023).
14. J. H. Churnside, V. V. Tatarskii, and J. J. Wilson, "Oceanographic lidar attenuation coefficients and signal fluctuations measured from a ship in the Southern California Bight," Appl. Opt. **37**(15), 3105–3112 (1998).
15. Y. Zhou, Y. Chen, H. Zhao, C. Jamet, D. Dionisi, M. Chami, P. Di Girolamo, J. H. Churnside, A. Malinka, and H. Zhao, "Shipborne oceanic high-spectral-resolution lidar for accurate estimation of seawater depth-resolved optical properties," Light: Sci. Appl. **11**(1), 261 (2022).
16. J. H. Churnside, J. W. Hair, C. A. Hostetler, and A. J. Scarino, "Ocean backscatter profiling using high-spectral-resolution lidar and a perturbation retrieval," Remote Sens. **10**(12), 2003 (2018).
17. J. D. Klett, "Stable analytical inversion solution for processing lidar returns," Appl. Opt. **20**(2), 211–220 (1981).
18. F. G. Fernald, "Analysis of atmospheric lidar observations: some comments," Appl. Opt. **23**(5), 652–653 (1984).
19. J. H. Churnside and R. D. Marchbanks, "Inversion of oceanographic profiling lidars by a perturbation to a linear regression," Appl. Opt. **56**(18), 5228–5233 (2017).
20. J. A. Schulien, M. J. Behrenfeld, J. W. Hair, C. A. Hostetler, and M. S. Twardowski, "Vertically-resolved phytoplankton carbon and net primary production from a high spectral resolution lidar," Opt. Express **25**(12), 13577–13587 (2017).
21. J. Hair, C. Hostetler, Y. Hu, M. Behrenfeld, C. Butler, D. Harper, R. Hare, T. Berkoff, A. Cook, and J. Collins, "Combined atmospheric and ocean profiling from an airborne high spectral resolution lidar," in *EPJ Web of Conferences*, (EDP Sciences, 2016), 22001.
22. A. Ansmann, M. Riebesell, and C. Weitkamp, "Measurement of atmospheric aerosol extinction profiles with a Raman lidar," Opt. Lett. **15**(13), 746–748 (1990).
23. Q. Liu, S. Wu, B. Liu, J. Liu, K. Zhang, G. Dai, J. Tang, and G. Chen, "Shipborne variable-FOV, dual-wavelength, polarized ocean lidar: design and measurements in the Western Pacific," Opt. Express **30**(6), 8927–8948 (2022).
24. D. J. Spence, B. R. Neimann, and H. M. Pask, "Monte Carlo modelling for elastic and Raman signals in oceanic LiDAR," Opt. Express **31**(8), 12339–12348 (2023).
25. M. Shangguan, H. Xia, C. Wang, J. Qiu, G. Shentu, Q. Zhang, X. Dou, and J.-W. Pan, "All-fiber upconversion high spectral resolution wind lidar using a Fabry-Perot interferometer," Opt. Express **24**(17), 19322–19336 (2016).
26. M. Shangguan, H. Xia, C. Wang, J. Qiu, S. Lin, X. Dou, Q. Zhang, and J.-W. Pan, "Dual-frequency Doppler lidar for wind detection with a superconducting nanowire single-photon detector," Opt. Lett. **42**(18), 3541–3544 (2017).
27. C. Yu, M. Shangguan, H. Xia, J. Zhang, X. Dou, and J.-W. Pan, "Fully integrated free-running InGaAs/InP single-photon detector for accurate lidar applications," Opt. Express **25**(13), 14611–14620 (2017).
28. A. Maccarone, A. Mccarthy, X. Ren, R. E. Warburton, A. M. Wallace, J. Moffat, Y. Petillot, and G. S. J. O. E. Buller, "Underwater depth imaging using time-correlated single-photon counting," Opt. Express **23**(26), 33911–33926 (2015).
29. A. Maccarone, F. Rocca, A. Mccarthy, R. Henderson, and G. S. J. O. E. Buller, "Three-dimensional imaging of stationary and moving targets in turbid underwater environments using a single-photon detector array," Opt. Express **27**(20), 28437–28456 (2019).
30. X. Shen, W. Kong, P. Chen, T. Chen, G. Huang, and R. Shu, "A Shipborne Photon-Counting Lidar for Depth-Resolved Ocean Observation," Remote Sens. **14**(14), 3351 (2022).
31. H. R. Gordon, "Interpretation of airborne oceanic lidar: effects of multiple scattering," Appl. Opt. **21**(16), 2996–3001 (1982).
32. U. Wandinger and A. Ansmann, "Experimental determination of the lidar overlap profile with Raman lidar," Appl. Opt. **41**(3), 511–514 (2002).
33. V. Gladkikh and R. Tenzer, "A mathematical model of the global ocean saltwater density distribution," Pure Appl. Geophys. **169**(1-2), 249–257 (2012).
34. J. S. Bartlett, K. J. Voss, S. Sathyendranath, and A. Vodacek, "Raman scattering by pure water and seawater," Appl. Opt. **37**(15), 3324–3332 (1998).
35. A. Bricaud, A. Morel, M. Babin, K. Allali, and H. Claustre, "Variations of light absorption by suspended particles with chlorophyllaconcentration in oceanic (case 1) waters: Analysis and implications for bio-optical models," J. Geophys. Res.: Oceans **103**(C13), 31033–31044 (1998).
36. A. Bricaud, A. Morel, and L. Prieur, "Absorption by dissolved organic matter of the sea (yellow substance) in the UV and visible domains1," Limnol. Oceanogr. **26**(1), 43–53 (1981).

Optics EXPRESS

37. A. Morel and S. Maritorena, "Bio-optical properties of oceanic waters: A reappraisal," J. Geophys. Res.: Oceans **106**(C4), 7163–7180 (2001).
38. Y. Huot, A. Morel, M. Twardowski, D. Stramski, and R. Reynolds, "Particle optical backscattering along a chlorophyll gradient in the upper layer of the eastern South Pacific Ocean," Biogeosciences **5**(2), 495–507 (2008).
39. H. Loisel and A. Morel, "Light scattering and chlorophyll concentration in case 1 waters: A reexamination," Limnol. Oceanogr. **43**(5), 847–858 (1998).
40. A. Morel, "Optical modeling of the upper ocean in relation to its biogenous matter content (case I waters)," J. Geophys. Res. **93**(C9), 10749–10768 (1988).
41. A. Morel, "Light and marine photosynthesis: a spectral model with geochemical and climatological implications," Prog. Oceanogr. **26**(3), 263–306 (1991).
42. L. Zotta, S. Matteoli, M. Diani, and G. Corsini, "AFRODiTE: A fluorescence LiDAR simulator for underwater object detection applications," IEEE Trans. Geosci. Remote Sensing **53**(6), 3022–3041 (2015).
43. A. Bricaud, M. Babin, A. Morel, and H. Claustre, "Variability in the chlorophyll-specific absorption coefficients of natural phytoplankton: Analysis and parameterization," J. Geophys. Res. **100**(C7), 13321–13332 (1995).
44. S. Maritorena, A. Morel, and B. Gentili, "Determination of the fluorescence quantum yield by oceanic phytoplankton in their natural habitat," Appl. Opt. **39**(36), 6725–6737 (2000).
45. C. D. Mobley, *Light and water: radiative transfer in natural waters* (Academic press, 1994).
46. A. Morel and L. Prieur, "Analysis of variations in ocean color 1," Limnol. Oceanogr. **22**(4), 709–722 (1977).
47. B. Bharathiraja, J. Jayamuthunagai, M. Chakravarthy, R. R. Kumar, D. Yogendran, and R. Praveenkumar, "Algae: Promising Future Feedstock for Biofuels," in *Algae and Environmental Sustainability* (Springer2015), pp. 1–8.
48. J. O'Reilly, "Status and trends in primary productivity and chlorophyll from 1996 to 2014 in large marine ecosystems and the Western Pacific warm pool, based on data from satellite ocean colour sensors," Intergovernmental Oceanographic Commission Technical Series **120**, 130 (2017).
49. T. Kostadinov, D. Siegel, and S. Maritorena, "Retrieval of the particle size distribution from satellite ocean color observations," J. Geophys. Res.: Oceans **114**(C9), C09015 (2009).
50. G. Campbell, S. R. Phinn, and P. Daniel, "The specific inherent optical properties of three sub-tropical and tropical water reservoirs in Queensland, Australia," Hydrobiologia **658**(1), 233–252 (2011).
51. A. Reinart, B. Paavel, D. Pierson, and N. Strömbeck, "Inherent and apparent optical properties of Lake Peipsi, Estonia," Boreal Environ. Res. **9**, 429 (2004).
52. S. Kratzer and G. Moore, "Inherent optical properties of the Baltic Sea in comparison to other seas and oceans," Remote Sens. **10**(3), 418 (2018).
53. J. Huang, X. Chen, T. Jiang, F. Yang, L. Chen, and L. Yan, "Variability of particle size distribution with respect to inherent optical properties in Poyang Lake, China," Appl. Opt. **55**(22), 5821–5829 (2016).
54. D. Ficek, J. Meler, T. Zapadka, B. Woźniak, and J. Dera, "Inherent optical properties and remote sensing reflectance of Pomeranian lakes (Poland)," Oceanologia **54**(4), 611–630 (2012).
55. Ø Frette, S. Rune Erga, B. Hamre, J. Aure, and J. J. Stamnes, "Seasonal variability in inherent optical properties in a western Norwegian fjord," Sarsia **89**(4), 276–291 (2004).
56. R. P. Souto, P. L. Silva Dias, H. F. Campos Velho, S. Stephany, and M. Kampel, "New developments on reconstruction of high resolution chlorophyll-a vertical profiles," Comp. Appl. Math. **36**(3), 1195–1204 (2017).
57. H. Loisel, D. Stramski, B. G. Mitchell, F. Fell, V. Fournier-Sicre, B. Lemasle, and M. Babin, "Comparison of the ocean inherent optical properties obtained from measurements and inverse modeling," Appl. Opt. **40**(15), 2384–2397 (2001).
58. J. Sánchez-España, C. Falagán, D. Ayala, and K. Wendt-Potthoff, "Adaptation of Coccomyxa sp. to extremely low light conditions causes deep chlorophyll and oxygen maxima in acidic pit lakes," Microorganisms **8**(8), 1218 (2020).
59. C. D. Mobley, "*Ecosystem Predictions with Approximate vs. Exact Light Fields*," (SEQUOIA SCIENTIFIC INC BELLEVUE WA, 2009).
60. S. Chen, P. Chen, L. Ding, and D. Pan, "A New Semi-Analytical MC Model for Oceanic LIDAR Inelastic Signals," Remote Sens. **15**(3), 684 (2023).
61. D. Liu, P. Xu, Y. Zhou, W. Chen, B. Han, X. Zhu, Y. He, Z. Mao, C. Le, and P. Chen, "Lidar remote sensing of seawater optical properties: experiment and Monte Carlo simulation," IEEE Trans. Geosci. Remote Sensing **57**(11), 9489–9498 (2019).
62. P. Chen, C. Jamet, Z. Mao, and D. Pan, "OLE: A novel oceanic Lidar emulator," IEEE Trans. Geosci. Remote Sensing **59**(11), 9730–9744 (2021).
63. T. J. Petzold, "*Volume scattering functions for selected ocean waters*," (Scripps Institution of Oceanography La Jolla Ca Visibility Lab, 1972).
64. A. Morel, D. Antoine, and B. Gentili, "Accounting for Raman emission and varying particle scattering phase function," Appl. Opt. **41**(30), 6289–6306 (2002).
65. L. Prieur and S. Sathyendranath, "An optical classification of coastal and oceanic waters based on the specific spectral absorption curves of phytoplankton pigments, dissolved organic matter, and other particulate materials 1," Limnol. Oceanogr. **26**(4), 671–689 (1981).
66. A. Morel, "Optical properties of pure water and pure seawater," Optical aspects of oceanography (1974).
67. Z. Lee and J. Tang, "The Two Faces of "Case-1" Water," J. Remote Sens. **2022**, 9767452 (2022).